Review Article

Yu Li, Jiachen Li, Hongchen Yu, Hai Yu, Hongwei Chen, Sigang Yang and Minghua Chen*

On-chip photonic microsystem for optical signal processing based on silicon and silicon nitride platforms

https://doi.org/10.1515/aot-2017-0057
Received September 5, 2017; accepted November 30, 2017; previously published online January 18, 2018

Abstract: The explosive growth of data centers, cloud computing and various smart devices is limited by the current state of microelectronics, both in terms of speed and heat generation. Benefiting from the large bandwidth, promising low power consumption and passive calculation capability, experts believe that the integrated photonics-based signal processing and transmission technologies can break the bottleneck of microelectronics technology. In recent years, integrated photonics has become increasingly reliable and access to the advanced fabrication process has been offered by various foundries. In this paper, we review our recent works on the integrated optical signal processing system. We study three different kinds of on-chip signal processors and use these devices to build microsystems for the fields of microwave photonics, optical communications and spectrum sensing. The microwave photonics front receiver was demonstrated with a signal processing range of a full-band (L-band to W-band). A fully integrated microwave photonics transceiver without the on-chip laser was realized on silicon photonics covering the signal frequency of up 10 GHz. An all-optical orthogonal frequency division multiplexing (OFDM) demultiplier was also demonstrated and used for an OFDM communication system with the rate of 64 Gbps. Finally, we show our work on the monolithic integrated spectrometer with a high resolution of about 20 pm at the central wavelength of 1550 nm. These proposed on-chip signal processing systems potential applications in the fields of radar, 5G wireless communication, wearable devices and optical access networks.

Keywords: integrated optics; microwave photonics; OFDM communications; optical signal processing; spectrometer.

1 Introduction

Over the past five decades, the rapid development of microelectronics technology has promoted the unprecedented progress of information technology (IT), such that the integrated circuit (IC) has even become the backbone of modern society. However, the microelectronics technology now suffers from a bottleneck in terms of heat generation and speed, and Moore's law is nearing the end [1]. Thus, there is a huge demand for such emerging technologies as the fast-growing fields of cloud computing, 5G wireless communications, Internet of things and so on. In the past decade, the integrated photonics has undergone rapid development similar to Moore's law [2]. Various photonic integration technologies based on different material platforms have been developed, and the three major ones are the silicon-on-insulator (SOI) waveguide technology, the III-V/InP generic integration and the silicon nitride-on-insulator waveguide technology [3]. A wealth of research efforts and investments from academic and industrial organizations (e.g. Intel, IBM, Huawei and so on) have also been carried out [4–6]. Similar to the era of microelectronics in the 1980s, the model of separating the design of the optical circuit and the system with the fabrication process based on the standard process design kit is being established [7, 8]. Access to the complex and state-of-art fabrication process is now made open to the public by many foundries around the world through the multi-project-wafer services or customized run, such as the IMEC, LETI, LioniX BV and HHI in Europe; IMECAS and IME in Asia; and AIM in the USA [9–13]. Thus, the integrated photonics is now widely accepted as the key technology that may enable microelectronics to break the

***Corresponding author: Minghua Chen,** Department of Electronic Engineering, Rohm Building, Tsinghua University, Haidian District, Beijing 100084, China, e-mail: chenmh@tsinghua.edu.cn
Yu Li, Jiachen Li, Hongchen Yu, Hai Yu, Hongwei Chen and Sigang Yang: Department of Electronic Engineering, Rohm Building, Tsinghua University, Haidian District, Beijing 100084, China

bottleneck of signal processing and transmission in terms of speed and power consumption. Such a technology can also open the doors for new applications, owing to the large bandwidth, low power consumption, parallel signal processing and inherent passive computing ability, such as the Mach-Zehnder interferometer (MZI)-based matrix multiplication [14].

In recent years, many typical woks on all-optical or electronic and photonic hybrid signal processing on-chip system, which is enabled by the advanced semiconductor manufacturing technology, have been proposed and demonstrated. For example, in 2012, the first large-scale photonic on-chip system of nanophotonic phased array with 4096 (64×64) optical nanoantennas was demonstrated; this system was fabricated in a 300-mm CMOS foundry with a 65-nm technology node [15]. This work marked the beginning of the large-scale integration of photonics and also promoted the research field of Lidar for the enormous demands in driverless car and unmanned aerial vehicle applications. In 2015, a microprocessor with 70 million transistors and 850 optical elements working together on a single chip was experimentally demonstrated for the first time, which was fabricated on IBM's commercial 45-nm process through the standard electronic design kit; this particular work introduced the monolithic electronic-photonic system [16]. In 2016, a fully integrated photonic network-on-chip circuit was reported, with a total transmission rate of 2.56 Tbps ($8\times8\times40$ Gbps) for interconnections based on the hybrid SOI and III/V integration technology. This work, which represented the maturity of heterogeneous integration, used over 300 active units (including 48 distributed feedback lasers) and over 120 passive units on a single chip [17]. In 2017, a photonic artificial neural network chip was proposed and implemented on a programmable nanophotonic processor, which was made up of 56 programmable MZIs based on SOI technology. The system achieved a feedforward neural network with two layers and was benchmarked on a vowel recognition problem with a comparable performance to a conventional 64-bit computer [18].

In this paper, we reviewed our recent works on the integrated optical signal processing system based on different waveguide technology platforms. Just like the transistor is the basic element of microelectronics, the MZI and micro-ring resonator are the basic elements that process and route the photons of the integrated photonics. Thus, we first discussed and presented the basic principle of MZI and micro-ring resonator and used the two elements to build three different types of on-chip optical signal processing units. Then, we utilized the processors to build different on-chip microsystems and applied these systems in the fields of microwave photonics, all-optical OFDM communications and spectrograph. In the application of microwave photonics, we utilized the infinite impulse response (IIR) filter as a signal processor to achieve a full-band RF photonic receiver. Further, the fully integrated RF photonic front transceiver on a single silicon photonics chip was experimentally demonstrated.

For the OFDM communications, a monolithic all-optical OFDM de-multiplexer based on the finite impulse response (FIR) signal processor in parallel with fixed phase relation was proposed and fabricated on SOI technology, with which an all-optical OFDM communication system was demonstrated. In the application of the spectrograph, multiple asymmetric MZIs in parallel with equidifferent differential path lengths were used to build the on-chip spectrometer based on the Si_3N_4/SiO_2 waveguide platform. The proposes system showed good balance among the high resolution, the robustness to fabrication tolerance and the compact size.

2 Signal processors on the integrated photonics

As stated in the introduction section, the MZI and ring resonator are the two basic elements for optical signal processing. Utilizing the two basic elements, the on-chip signal processors based on different schemes have been studied in recent years. For example, Marpaung et al. [19] experimentally demonstrated the first integrated MWP bandstop filter based on the stimulated brillouin scattering (SBS) process, and reported a high suppression of more than 55 dB, a high resolution of about 50 MHz and a frequency tuning range of 0–30 GHz. Recently, the concept of a fully reconfigurable photonic integrated signal processor inspired by the FPGA in electronics has been proposed and demonstrated on different waveguide platforms [20, 21]. The presented optical signal processors can be divided into two types. One is the nonlinear process assisted device that can achieve excellent performance on certain characteristics, such as the filtering linewidth; however, it often needs a specific optimization of the fabrication process and is power dependent. The other one is the linear component, which is power independent, and is most widely used due to the advantages of low fabrication cost, easy design and programmability.

In this section, we focus on the type of linear devices. In principle, these integrated optical signal processors can be divided into three different types [22]: (1) FIR filters, the performance of which depends on the number of taps

and the corresponding weights and the phase response is linear; (2) IIR filters, which have feedback loops and a phase jump at the resonant frequency and (3) FIR/IIR hybrid filters, which usually consist of feedback loops and taps simultaneously. Our recent works on these three kinds of signal processors are presented in this section.

2.1 FIR signal processor

FIR signal processors have the advantages of stability, linear phase response and insensitivity to the fabrication tolerance. In general, two schemes are used to realize the FIR filter in the optical domain. One is to divide the light into multiple paths with different delays and different attenuations, and then combine the beams of light together again. The other architecture is based on the traditional MZI, whose free spectral range (FSR) has an inverse relation with the differential path length of the two arms and is about twice the bandwidth. Due to the mutual restraint between the narrow bandwidth and large FSR, a single FIR filter cannot be used in many applications. Many different schemes to deal with the problem have been proposed [23–25].

In our work, we presented a narrow-bandwidth FIR processor based on multistage cascaded MZIs [26, 27]. Figure 1 shows the schematic diagram of the FIR processor, with each MZI unit tuned individually. In order to ensure the accuracy of the filter, this structure also enlarges the FSR of the processor, which greatly expands the range of application. As shown in Figure 1, the differential path lengths of the two arms of the MZIs on each stage are respectively expressed as $\Delta L_1 = L$, $\Delta L_2 = 2^{-1}L, \ldots$, $\Delta L_N = 2^{-(N-1)}L$. The transmission function of the system is given by [26].

$$H = \Pi_{(i=1)}^{N}\left(\sqrt{1-\kappa_{2i-1}}\sqrt{1-\kappa_{2i}}e^{j\phi_i} - \sqrt{\kappa_{2i-1}}\sqrt{\kappa_{2i}}\gamma_i e^{-j\beta(2^{-(i-1)}L)}\right), \quad (1)$$

where β and ϕ_i are the propagation constant in the waveguide and the phase difference of the two arms, respectively. To reduce the insertion loss of the passband and increase the contrast ratio of the MZI, the coupling coefficient of each coupler is set to be $\kappa_{2i-1} = \kappa_{2i} = (1+\gamma_i)^{-1}$, which makes all the zeros of the system on the unit circle. As the same time, we also set $\phi_i = \pi$, which means that an extra π phase shift is introduced for each stage. Thus, all the resonance frequencies of the MZIs can be aligned at a certain frequency. At such condition, Equation (1) is given by

$$H \propto (-1)^N (1+z^{-2^{(N-1)}})(1+z^{-2^{(N-2)}})(1+z^{-2^{(N-3)}})\ldots(1+z^{-1}), \quad (2)$$

where $z = e^{j\Omega}$ and $\Omega = \beta \cdot 2^{-(N-1)}L$. The zeros of such an FIR processor with three-stage cascaded MZIs are distributed uniformly on the unit circle. The FSR of the processor is decided by the differential path lengths of the final stage, whereas the bandwidth of the processor is mainly determined by the first stage and becomes slightly reduced as the number of stages increase. In addition, the zeros of the system would rotate on the unit circle by tuning the phase difference of the two arms of each stage. Thus, the profile of the transmission function changes as the zeros rotate. This means that the multistage cascaded MZI-based filter is a programmable and reconfigurable FIR processor.

The three major integrated photonics platforms are the SOI, InP and Si_3N_4 waveguide technologies. Among these platforms, the SOI technology has the great advantages of high compactness, low fabrication cost in large volumes and a diverse range of passive and active devices. Thus, we implemented the proposed FIR processor first on the SOI technology platform. The device was fabricated by the SOI waveguide technology, which was initially offered by LETI [9]. Based on a 193-nm ultra-violet (UV) lithography, the waveguide was processed to be trip waveguide with a width of 450 nm and a thickness of 220 nm. The heaters and electrical contact pads, which consisted of 110 nm Ti/TiN, were deposited on the waveguides with a 600-nm thick silica layer as the interlayer. The propagation loss of the strip waveguide was about 3.0 dB/cm. The bend loss was negligible and the bend radius was more than 5 μm.

In the numerical study, the differential path lengths of the two arms of the first stage were set to be L = 2.98 cm. The transmission spectra of the FIR processors with N = 1, N = 3 and N = 5 stages were calculated. The results are shown in Figure 2. When N = 1, the FSR of the FIR processor is about twice its bandwidth. As the number of the stages increase,

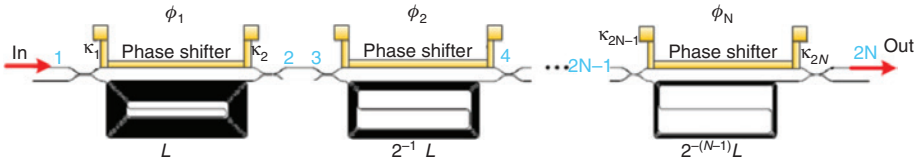

Figure 1: The schematic diagram of the proposed cascaded MZI-based FIR processor with N stages.

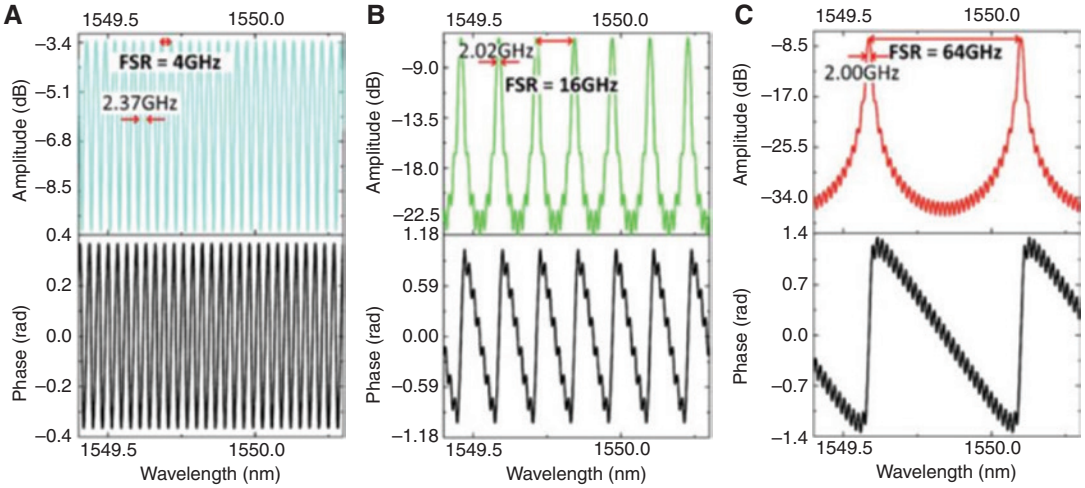

Figure 2: The numerical study of the amplitude and phase response of the multi-stage cascaded MZI filter. (A) N = 1, (B) N = 3, (C) N = 5.

the bandwidth of processor slightly decreases, whereas the FSR is enlarged by 2^{N-1} times. The extinction ratio is also improved from 6.5 dB to 30 dB when the number of the stage is from 1 to 5. In addition, all the phase responses of the processors in the three conditions are linear. The numerical results agree well with the theory.

In the experiment, a three-stage cascaded MZI-based FIR processor was fabricated with a size of about 1.4 mm × 3 mm. The processor is shown in Figure 3A. We used an optical vector analyzer (OVA) with a resolution of 1.25 pm to measure the transmission function of the device as shown in Figure 3B. In order to realize the target transmission spectrum of the proposed processor, such as the single-channel filter at the wavelength of 1550 nm, we tuned the voltages applied to the three heaters fabricated on the MZIs using real-time OVA. In addition, a Peltier module was utilized to stabilize the temperature to 0.1 K. All the demonstrated devices introduced in this paper were implemented with the similar control method to achieve the target transmission function. The measured bandwidth

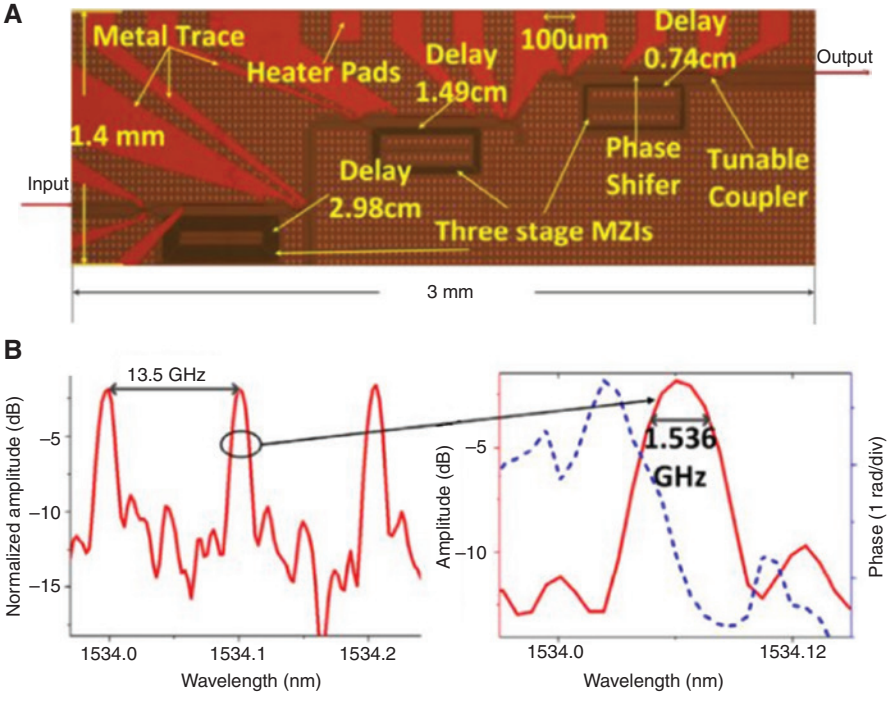

Figure 3: The experimental result of the three-stage cascaded MZI based FIR processor. (A) The picture of the fabricated FIR processor with three stages and (B) the measured transmission spectrum.

and FSR of the processor were about 1.54 GHz and 13.5 GHz, respectively. Both bandwidths meet the requirement for a processing bandwidth from X-band to Ka-band in microwave photonics at the wavelength of 1534 nm. The measured phase response is linear. Further, the extinction ratio of the processor is slightly lower than the numerical result, which may be due to the fabrication tolerance.

Until now, the best performance of the SOI waveguide platform on the propagation loss is about 1 dB/cm [28], which makes it difficult for an SOI technology-based FIR processor to realize a bandwidth below 1 GHz. However, many applications require a signal processor with a processing bandwidth at the level of 100 MHz, such as in microwave photonics, wireless communications and so on. Therefore, we took advantage of the TriPleX™ waveguide technology offered by LioniX BV, which was founded in the Netherlands. Compared with the SOI waveguide technology, the greatest advantage of the TriPleX™ technology is the very low loss of 0.1 dB/cm [29]. The proposed FIR processor was fabricated on the double-strip TrIPleX™ waveguide platform. The double-strip waveguide consisted of three successive layers (Si_3N_4, SiO_2 and Si_3N_4 layers) in the vertical direction. The corresponding thicknesses of the three layers are 170 nm, 500 nm and 170 nm, respectively, as shown in Figure 4A. The typical width of the waveguide is 1.2 μm, and the corresponding effective index and the group index of the TE0 mode are about 1.535 and 1.71, respectively, at a wavelength of 1550 nm. The mode profile of the TE0 mode is shown in Figure 4B.

Based on the TriPleX™ waveguide technology, we experimentally demonstrated a programmable and reconfigurable FIR processor with three-stage cascaded MZIs [30]. The highest signal processing accuracy of the processor is about 140 MHz. By cascading a micro-ring based IIR filter, the overall system can achieve a processing range of more than 112.5 GHz. The architecture (shown in Figure 5A) of the processor is similar to the aforementioned processor based on the SOI technology. In the current work, the symmetric MZI in each stage was used to adjust the signal distribution ratio to improve the contrast ratio of the corresponding asymmetric MZI. The longest differential path was designed to be 50 cm to realize a narrow bandwidth of about 100 MHz; hence, the differential path lengths of the remaining two stages were 25 cm and 12.5 cm, respectively. The processor had 7 zeros and the distribution of the zeros could be changed by tuning the phase shifter of the MZI on each stage, which can then determine the transmission spectrum of the processor. The numerical results show three different filter profiles by adjusting the distributions of the zeros. These profiles correspond to the unimodal filter, the bimodal filter and the quad peak filter, as shown in the dashed lines in Figures 5B–D, respectively. Such an FIR processor with a flexible reconfigurable feature can be widely applied in signal extraction and in signal shaping.

The size of the fabricated device, shown in Figure 6A, was about 32 mm × 3.25 mm. Given that the resolution of the OVA is 150 MHz, it is unable to measure the FIR processor with a bandwidth of about 100 MHz. We used the RF vector network analyzer (VNA) based on the microwave photonics technology to set up a tunable high-precision optical vector analysis system. The detailed principle of the measurement is presented in a previous work [30]. By tuning the phase heater, the measured transmission spectrum (red lines in Figures 5B–D) can be almost identical to the numerical result (black dashed lines in Figures 5B–D). In the application of signal extraction, such as in wireless communications, the FIR processor can be applied as a single-channel or dual-channel filter. Their corresponding transmission spectra are shown in Figures 6B and C, respectively. For the single-channel filter, the measured bandwidth could be tuned from 143 MHz to more than 300 MHz, as shown in Figure 6B. Figure 6C shows that the channel spacing between the two peeks of the dual peak filter is altered from 200 MHz to about 700 MHz, whereas

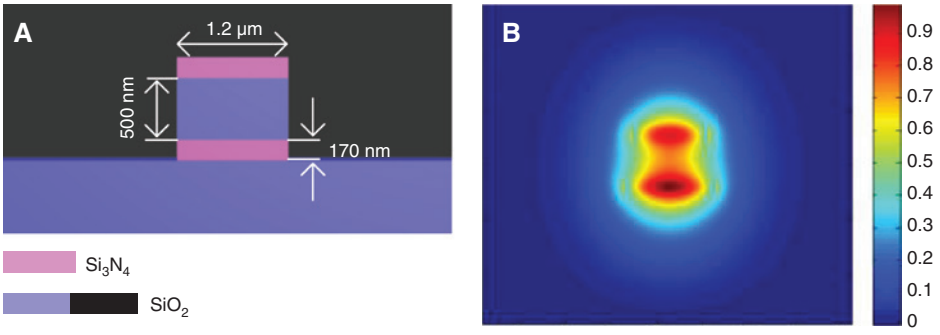

Figure 4: The characteristic of the double-strip TriPleX™ waveguide technology. (A) The cross-section and (B) the TE0 mode profile at wavelength of 1550 nm.

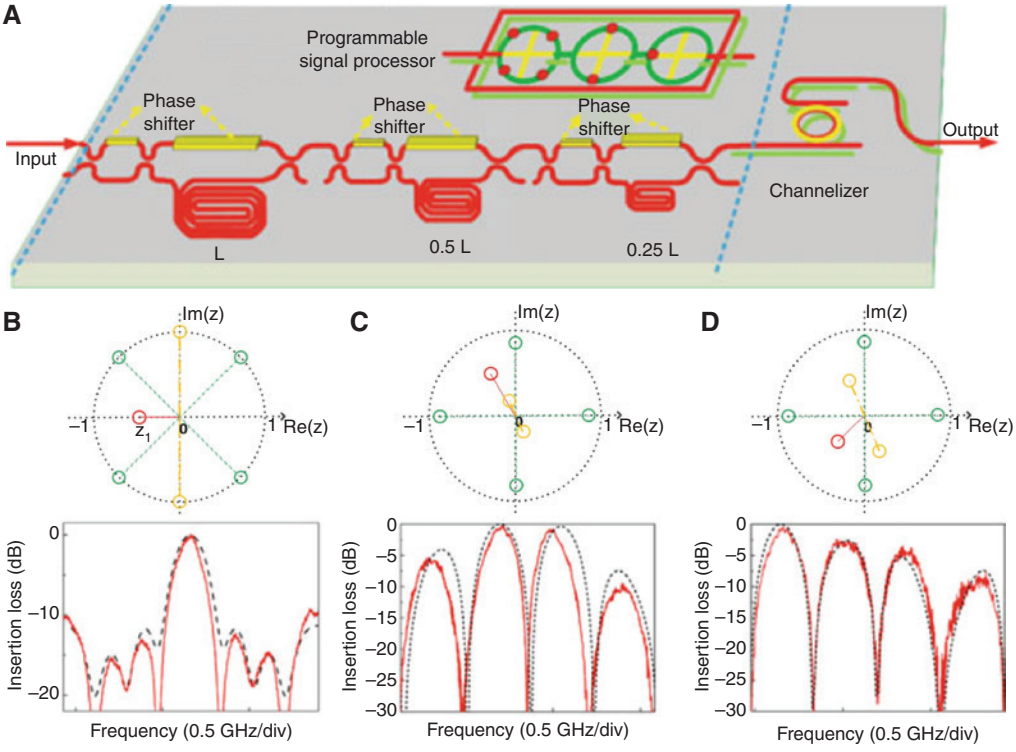

Figure 5: The characteristic of the FIR processor with three-stage cascaded MZIs based on TriPleX™ waveguide technology. (A) The schematic diagram of the FIR processor and (B–D) the transmission spectra of the processor at different zero distributions (top) both in simulation (bottom, black dashed line) and experiment (bottom, red line).

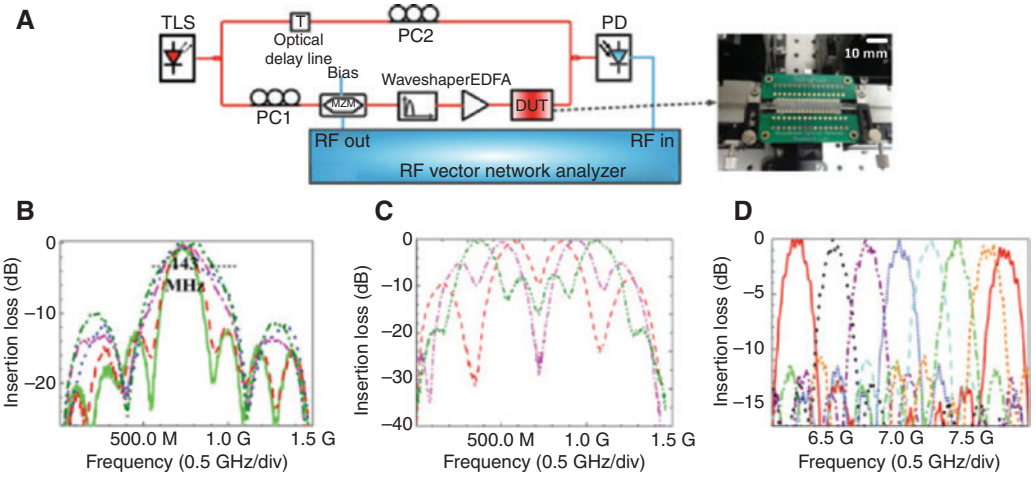

Figure 6: The experimental result of the fabricated FIR processor. (A) The schematic diagram of the measurement system based on the microwave technology and (Right) the picture of the fabricated chip; (B) the single band response, (C) the dual pass band response and (D) the thermally tuning response.

the bandwidth is almost unchanged. In addition, the central wavelength of the FIR processor can be thermally tuned based on the temperature electric control (TEC) module, which has a tuning ability of about 2 GHz/K, as shown in Figure 6D. In principle, the FSR of a three-stage cascaded MZI-based FIR processor is limited to be 4 times larger than a single MZI filter. Thus, we added an IIR filter as a channel filter with large FSR to further enlarge the signal processing range of the processor to 110 GHz.

In summary, a multistage cascaded MZI-based FIR signal processor has the advantages of programmable and linear phase response. By increasing the number of stages, the FIR processor can realize a very narrow bandwidth with high signal processing accuracy. The profile of

the transmission spectrum can also be changed for different applications. However, the weakness of such processor is that the FSR and the bandwidth are almost of the same order of magnitude, which limits the signal processing range. To deal with the problem, cascading a micro-ring resonator with large FSR is a good solution.

2.2 IIR signal processor

An integrated IIR processor is typically implemented using micro-rings, micro-spheres, or photonic crystal micro-cavities, so that such processor can be realized in a compact size [31–33]. In general, the bend loss of the SOI waveguide with a radius of several microns is negligible, so that the size of micro-ring based IIR processor can be down to a few microns [34]. If the IIR processor is built on a photonic crystal platform, the total size is just one micron [35]. With such a compact structure, the FSR of the IIR processor is commonly large. For example, the FSR of a micro-ring based on SOI technology can be as large as tens of nanometers [34]. Owing to the nature of the structure, the intrinsic Q value of the micro-ring filter is determined only by the waveguide loss. Thus, an IIR processor with a very high Q value can be achieved on a low-loss waveguide platform in a small footprint [36], which can realize ultra-high precision signal processing and cover a processing range of a few nanometers.

The two basic frameworks of the micro-ring resonators are the all-pass ring resonator and the add-drop ring resonator, as shown in Figure 7. For the all-pass ring resonator, only the optical light at specific wavelength can circulate in the ring, thus causing a tip in the transmission spectrum, as shown below

$$\mathrm{T}=\frac{E_{\mathrm{thr}}}{E_{\mathrm{in}}}=(t-e^{-j\beta L_c}e^{-\alpha L_c/2})/(1-te^{-j\beta L_c}e^{-\alpha L_c/2}), \tag{3}$$

where t is the self-coupling coefficient with respect to the electric field, β is the propagation constant of the optical mode, α is the power attenuation coefficient and L_c is the round-trip length of the ring resonator. As for the add-drop ring resonator, the incident light can be partially transmitted to the drop port at the resonance wavelength. The transmission functions of the through port and pass port are respectively given by

$$T_{\mathrm{thr}}=\frac{E_{\mathrm{thr}}}{E_{\mathrm{in}}}=(t_1-t_2e^{-j\beta L_c}e^{-\alpha L_c/2})/(1-t_1t_2e^{-j\beta L_c}e^{-\alpha L_c/2}), \tag{4a}$$

$$T_{\mathrm{drop}}=\frac{E_{\mathrm{drop}}}{E_{\mathrm{in}}}=-(\kappa_1\kappa_2e^{-j\beta L_c/2}e^{-\alpha L_c/4})/(1-t_1t_2e^{-j\beta L_c}e^{-\alpha L_c/2}), \tag{4b}$$

where κ is the cross-coupling coefficient, and satisfies $\kappa^2+t^2=1$ with the assumption of energy conservation.

Our recent work on an IIR signal processor was mainly applied in microwave photonics. To cover the full-band RF signal processing from the L-band to the W-band (110 GHz in total) in the RF photonic front, the FSR of the processor must be about 220 GHz considering the double-sideband modulation and the bandwidth of less than 1 GHz. For the micro-ring resonator, the FSR and the intrinsic Q value satisfy the equations respectively given by

$$\mathrm{FSR}=\frac{\mathrm{c}}{\mathrm{n_g L}}, \tag{5}$$

$$\mathrm{Q_{int}}=\frac{2\pi \mathrm{n_{eff}}}{\lambda\alpha}. \tag{6}$$

As the propagation loss on the SOI platform is about 3 dB/cm, the calculated intrinsic Q value and the corresponding bandwidth are 1.35×10^5 and 1.4 GHz, respectively, at the wavelength of 1550 nm. The bandwidth of the IIR processor fabricated on the SOI waveguide does not satisfy the requirement. Therefore, the TriPleX™ waveguide technology was still used for processing the IIR processor in our work. Based on Equation (4), the intrinsic Q value and the corresponding bandwidth were calculated to be 2.7×10^6 and 70 MHz at the wavelength of 1550 nm, respectively. Considering that the bend loss can be negligible with a radius of more than 70 μm, the radius of the micro-ring filter was designed to be a typical value of 125 μm. The corresponding FSR of the filter with such a size was calculated to be 223 GHz based on Equation (3), thus meeting the requirement for a full-band RF signal processing.

Based on the TriPleX™ technology, we fabricated an add-drop micro-ring filter with a radius of 125 μm (shown in Figure 8A); the gaps between the bus waveguides and ring resonator were both 2 μm [37, 38]. Using the same

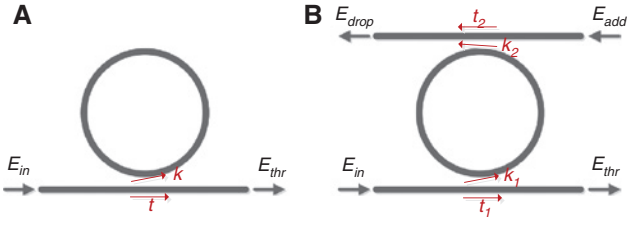

Figure 7: The two basic frameworks of the micro-ring resonators. (A) all-pass ring resonator and (B) the add-drop ring resonator.

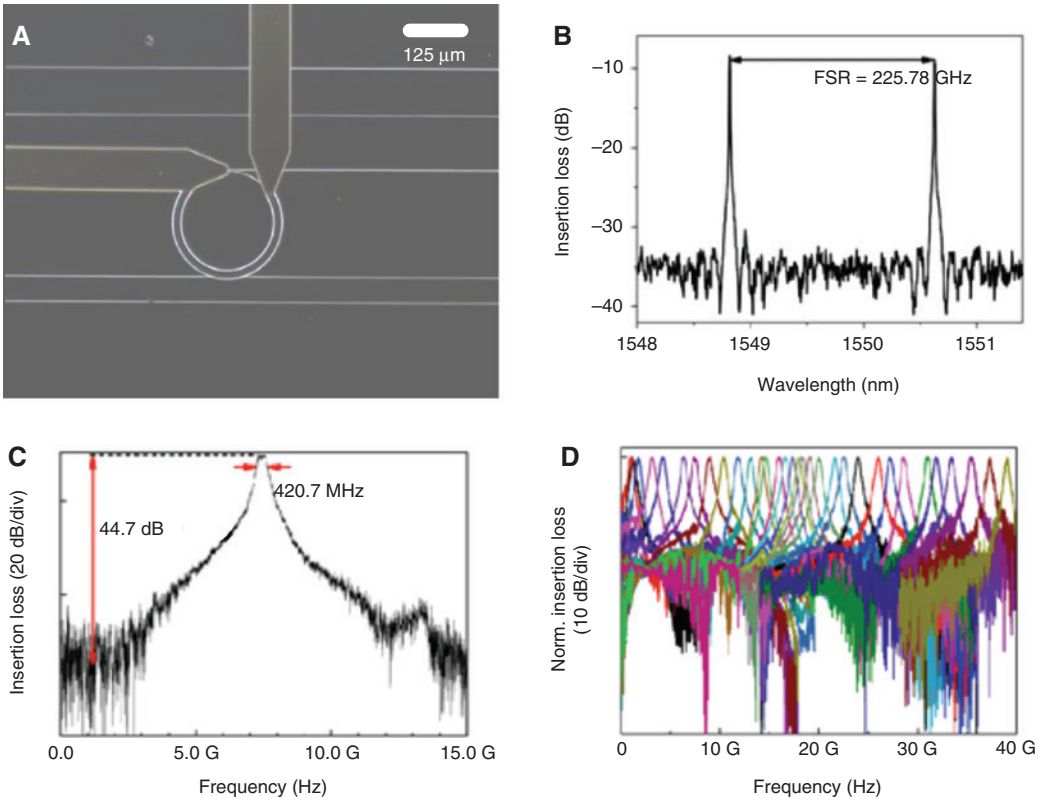

Figure 8: The experimental result of the fabricated IIR processor. (A) The micrograph of the fabricated IIR processor with the heater on the top and (B) the corresponding transmission spectrum measured by OVA, which shows the FSR of the filter is about 226 GHz; (C) the measured result by the VNA-based measurement system and (D) the thermal tuning response of the processor at different heater power changed from 0 mW to 110 mW.

VNA-based measurement system as the FIR processor based on the TriPleX™ technology, we measured the FSR of the IIR processor of about 220 GHz at the wavelength of 1550 nm, as shown in Figure 8B. Figure 8C shows that the measured linewidth and out-of-band suppression ratio are about 420 MHz and more than 40 dB, respectively, at the same wavelength. By thermally tuning the heater fabricated on the micro-ring filter, a wide tuning range of more than 40 GHz is realized, as shown in Figure 8D. The thermal tuning ability was measured to be around 350 MHz/mW.

2.3 FIR/IIR hybrid signal processor

The hybrid signal processors have potential for more flexible programmability as there are both zeros and poles in the filtering system. To further improve the Q-value of the filter and reduce the bandwidth, a potential method for the high-resolution signal processor based on the electromagnetically induced transparency (EIT)-like effect has been proposed [39]. The transmission function is indicated by

$$H=-(\kappa_1-\kappa_2 e^{-\beta_1 L_1})(\kappa_1-\kappa_2 e^{-\beta_2 L_2})/[\kappa_1\kappa_2(e^{-\beta_1 L_1}+e^{-\beta_2 L_2}) +t_1^2 t_2^2 e^{-2\beta_b L_b-0.5\beta_1 L_1-0.5\beta_2 L_2}-\kappa_1^2\kappa_2^2 e^{-\beta_1 L_1-\beta_2 L_2}-1], \quad (7)$$

where κ_i is the cross-coupling coefficient and t_i is self-coupling coefficient with respect to the electric field, both satisfying $\kappa_i^2+t_i^2=1$. In addition, β_i is the complex propagation constant of the optical mode, which includes the power attenuation coefficient of the waveguide.

The signal processor composed of the two-ring resonators with slightly different sizes is shown in Figure 9. In this structure, three resonances exist: the two ring resonances and the Bragg resonance induced by the two rings. Generally, the three resonances are the same under the condition of $L_{c1}=L_{c2}=2L_b$, where L_{ci} is the circular path of the ith ring and L_b is the distance between the two rings. In this design, a slight detuning is introduced between the two rings, indicating $\lambda_1\neq\lambda_2\approx\lambda_b$, where λ_i is the resonance wavelength of the i_{th} ring and λ_b is the resonance wavelength of the Bragg resonance, to utilize the EIT-like effect in the two-ring structure, thus achieving a Q-enhanced resonance.

Figure 10A shows the simulation of the transfer response of the EIT-like effect, which exhibits a narrow resonance tip in the notch band of the two-ring resonances.

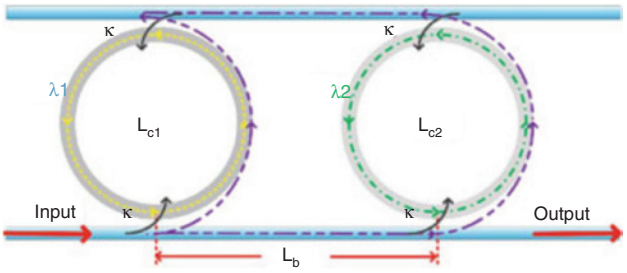

Figure 9: The schematic diagram of the EIT-like effect-based Q-enhanced bandpass filter with the two ring resonators.

As can be seen, the transfer response is not a simple product of the two cascaded rings. The phase response is shown in Figure 10B. At the point of the resonance tip, the phases of ring I and ring II have equal magnitude and opposite sign, which change the response from destructive interference to constructive interference, thus creating the bandpass channel (Figure 10). This is why the sideband suppression is enlarged and the bandwidth is narrowed with a Q-enhancement. In addition, with the method of adjusting the detuning between the two rings, a bandwidth tunable filter can also be achieved.

Figure 11 shows the variation of the bandwidth and Q-enhancement of the EIT-like effect with the waveguide loss ranging from 0 to 5 dB/cm for the adopted waveguide of 450 nm width and 220 nm height, the loss of which is about 3 dB/cm. The Q-enhancement of our proposed filter is inversely proportional both to the waveguide loss and to the bandwidth of the single ring. With proper design, the Q-enhancement can be as much as two orders of magnitude higher, as shown in Figure 11B. As the resonance tip of the EIT-like effect is near the notch bands, the value of Q-enhancement becomes larger under the condition of critical coupling with the deepest notch. In this situation, the depth of the notch can reach nearly –30 dB. The SOI platform mentioned above offered by LETI was used to fabricate the device and the performance was measured as shown in Figure 12.

The measured bandwidth of the filter is about 4.8 GHz and the sideband suppression ratio is about 15.7 dB, which is limited by the noise floor of the OVA, as shown in the inset of Figure 12A. The Q-value of the single ring under this proposed condition is only 1409, whereas the Q of the filter based on the EIT-like effect is as high as 38 750. Thus, the enhancement of Q is about 27. Meanwhile, we

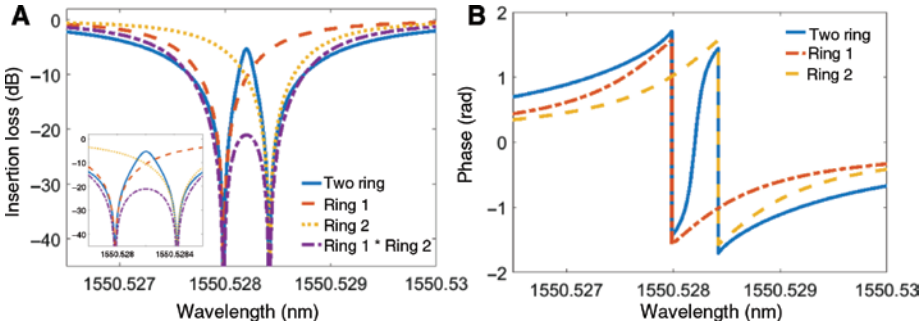

Figure 10: The diagram of the EIT-like effect-based Q-enhanced bandpass filter. (A) Q-enhanced EIT-based filter compared with the product of the two detuning rings. The inset shows the enlargement transmission spectrum around the resonance wavelength. (B) Phase response of the proposed filter.

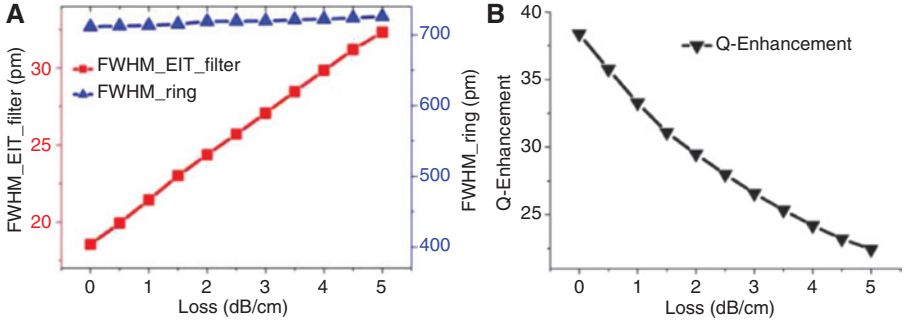

Figure 11: The influence of the waveguide loss on the FWHM and Q-enhancement. (A) The FWHMs of the EIT-based Q-enhanced filter and the single ring with different loss coefficients of the waveguides. (B) The Q-enhancement changes with waveguide loss.

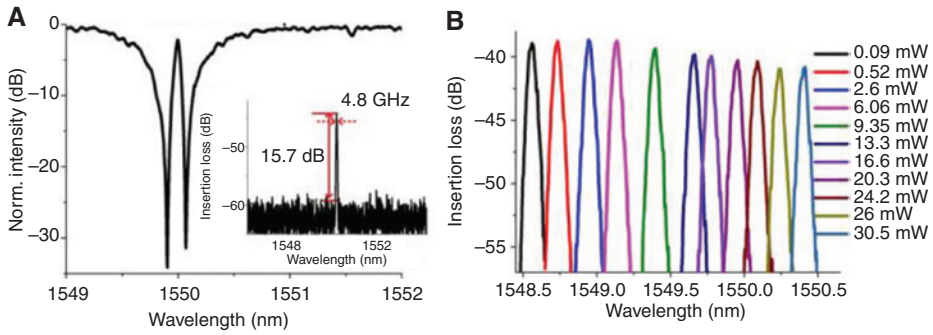

Figure 12: The performance of the proposed Q-enhanced filter. (A) The measured Q-enhanced filter response. The inset is the response after a channelizer. (B) The passband of the proposed filter shifted with different dissipation input electrical power.

can use a semiconductor cooler to realize the tuning of the center wavelength of the filter, as shown in Figure 12B. The proposed filter fabricated on the SOI platform achieved a Q-enhancement of 27, but its bandwidth is only 4.8 GHz. From the above analysis, it could be seen that the low-loss silicon nitride waveguide can be utilized to further improve the Q-value.

Due to the low loss of the TriPleX™ waveguide technology, we further experimentally demonstrated the EIT-like effect signal processor on the platform. The performance was measured with the resolution measurement system based on VNA as introduced in Section 2.1. The measured 3-dB bandwidth of the transparent window can be adjusted from 2.2 MHz to 10 MHz, as shown in Figure 13, indicating that the Q-value of the filter changes from 8.7×10^7 to 2×10^7. The Q-enhancement could reach 200. As far as we know, this is the highest reported Q-value. As shown in Figure 13B, the insertion loss for 10 MHz bandwidth is –15 dB.

In this section, we study the high-Q filter response based on the EIT enhancement effect between rings, and show the demonstrated filters, with bandwidths of 4.8 GHz and less than 10 MHz on the SOI platform and the TriPleX™ platform, respectively. These values correspond to the Q-enhancement of 27 and 200 on the respective platforms. However, we need to find a compromise between the bandwidth and insertion loss in practical application. This would be a promising method to achieve an ultra-high Q integrated compact filter for critical applications.

3 Microwave photonics fronts

With the rapid development of mobile Internet, satellite networking and broadband phased array for radar, the requirements for microwave front are mainly focused on the performance of the configurability and the multi-band signal processing capability as well as on the expansion of the working band to microwave millimeter [40, 41]. The photonic means of the RF photonic receivers/front-ends can potentially meet these requirements due to the advantages of flexible tunability, large bandwidth and immunity to electromagnetic interference [42, 43]. Thus, microwave photonics has increasingly attracted interest in recent years [44–48]. In this section, we first reviewed our work on full-band (from the L-band to the W-band) all-optical RF receiver based on the IIR processor fabricated on the

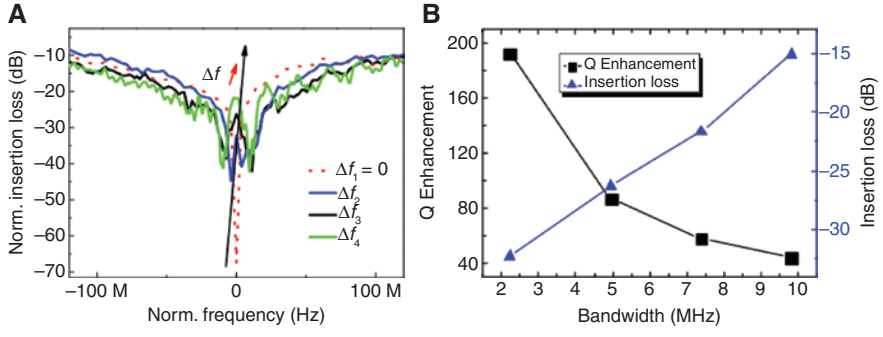

Figure 13: The tunable performance of the EIT-like filter based on the TriPleX™ waveguide technology. (A) The transfer response for the different frequency detuning between the two microrings, (B) The enhancement of the Q-value and the insertion loss.

TriPleX™ technology, which has been introduced in Section 2.2. On this basis, we further experimentally demonstrated a fully integrated microwave photonics front consisting of electro-optical (EO) modulator, signal processor and detector on the same chip except for the laser. Based on the microsystem, the optical RF transceiver was demonstrated, including the RF up-conversion and down-conversion unit, the local frequency comprehensive unit, the signal phase shifter unit and the signal processor unit. This work is a step forward towards the development of monolithic microwave photonics on silicon platform.

3.1 Full-band RF photonic receiver

Figure 14 shows the system architecture of the proposed full-band all-optical RF receiver. A continuous wave (CW) laser with narrow linewidth at the wavelength of 1550 nm was launched into the system and divided into two beams to act as the optical carrier. One was for the RF LO, and the other one was for the received RF signal. By carrier-suppressed modulation via a null-biased MZM, the RF LO was up-converted to the optical domain. Similarly, the received RF signal was up-converted by a phase modulator. Owing to the two modulators' sensitivity to the polarization of the optical signal, the polarization controllers (PC) were necessary here. An EDFA was also needed to amplify the modulated RF signal from the phase modulator before the signal was sent into the on-chip IIR processor. This is typically used to compensate for the optical loss of the system, which is mainly caused by the coupling loss between the fiber and the chip. The total loss between the fiber and the chip for a single frequency signal at the pass band of the IIR processor is about 8 dB, which includes twice the coupling loss of about 5 dB. Afterwards, the signal is sent to the proposed IIR processor to extracted the target signal with a processing bandwidth of 420 MHz. The extracted target signal is then combined with the RL LO, which is up-converted to optical domain and propagate through a delay line at a 1:1 coupler and detected by the balanced photo detector (BPD) for down converting. Thus, the extracted target signal comes back to the electrical domain and can be furthered processed by the backend systems, such as DAC, DSP and so on. Based on the IIR processor with narrow bandwidth and high rejection ratio out of the pass band, the target signal can be extracted clearly without any other interference sidebands, which would increase the spurious free dynamic range (SFDR) and reduce the nonlinear effect. In principle, the signal processing range of the system is limited by the FSR of the IIR processor and the bandwidth of the modulation. As stated in Section 2.2, the FSR of the processor is more than 220 GHz so that the processing range is determined by the modulation. Considering that the bandwidth of commercial modulation is up to 110 GHz, the system has the potential to cover the full band from 1 GHz to 110 GHz.

In the experiment, the performance of the system within the signal processing ranging from the L-band to the Ka-band (limited by the bandwidth of the modulator) was measured. The optical power of the CW laser used for the optical carrier was 16.7 dBm. The bandwidths of the two modulators were both 40 GHz. The gain of the EDFA for amplifying the signal from the PM modulator was 20 dB. The power of the RF LO was 20 dBm, and the corresponding carrier-suppression ration was larger than 20 dB. We used two-tone signal as the received signal ranging from the L-band to the Ka-band. By tuning the center wavelength of the narrow-band IIR processor with 40 dB rejection ratio out of the band, the system can extract the received signal at the first order of the modulated sideband in optical domain. By the subsequent down-conversion via BPD, we thus acquired the received signal accurately.

To further evaluate the linearity of the system, the SFDR at the processing ranging from L-band to Ka-band

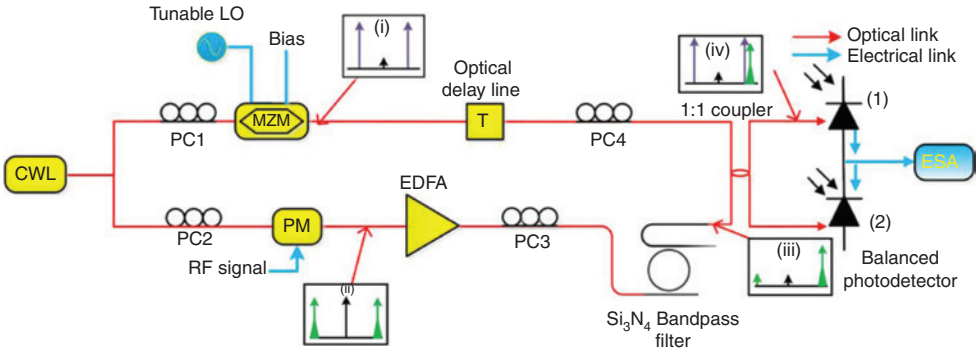

Figure 14: The schematic diagram of the RF photonic receiver using the demonstrated IIR filter as the signal processor.

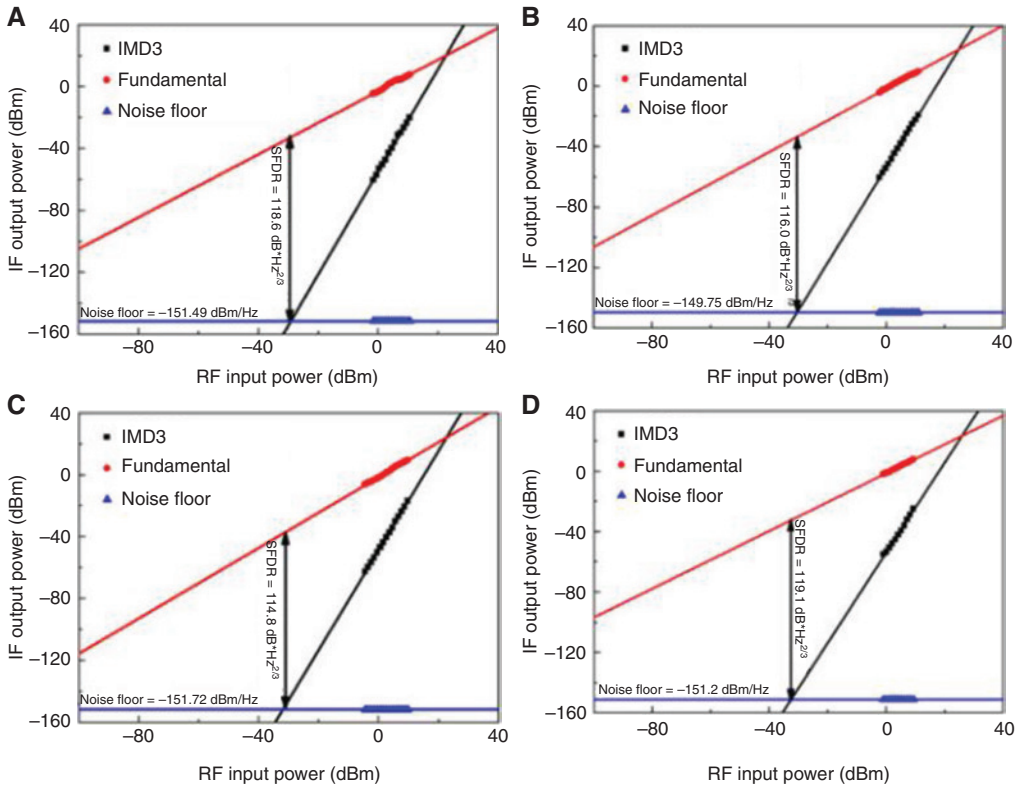

Figure 15: The measured SFDR of the RF photonics receiver from the C-band to the K-band. (A) C-band, (B) X-band, (C) Ku-band and (D) K-band.

was measured. The nonlinearity of the system is mainly caused by the PM modulation and the BPD; hence, the received signal launched into the BPD consists of the first-order sideband and the three-order cross-modulation nonlinear signal (IMD3). With the spectrum analyzer set as follows: RBW = 1 kHz, VBW = 1kHz, AT = 30 dBm, the measured SFDR at the frequency ranging from C-band to K-band is shown in Figure 15. The noise floor of the measurement set-up was about –151 dBm/Hz, which was mainly determined by the amplified spontaneous emission (ASE) noise of the EDFA. The measured SFDR values of the C-band (Signal: 4.8065 and 4.8085 GHz, IF: 6.5 and 8.5 MHz), the X-band (Signal: 10.0065 and 10.0085 GHz, IF: 6.5 and 8.5 MHz), Ku-band (Signal: 13.5065 and 13.5085 GHz, IF: 6.5 and 8.5 MHz) and the K-band (Signal: 19.0065 and 19.0085 GHz, IF: 6.5 and 8.5 MHz) are 118.6 dB-Hz$^{2/3}$, 116.0 dB-Hz$^{2/3}$, 114.8 dB-Hz$^{2/3}$ and 119.1 dB-Hz$^{2/3}$, respectively.

The SFDRs, noise factor and conversion gain of the system at the frequency ranging from 1.5 GHz to 39.5 GHz with a spacing of 2 GHz were also measured, as shown in Figure 16. In the measured frequency range, the performance of the system shows good uniformity with a slight fluctuation of less than 10 dB for the SFDR. Thus, the system can work well at a higher frequency band based on the same principle.

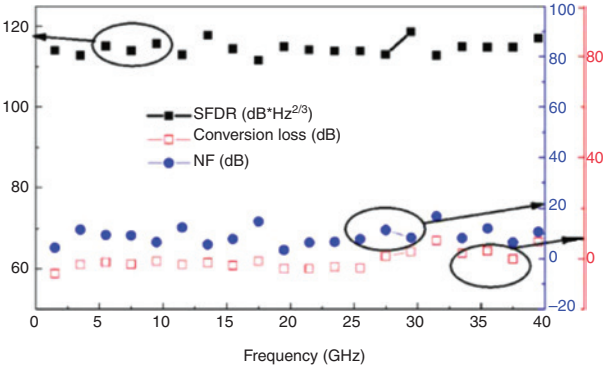

Figure 16: The measured result of the performance on the SFDR (black solid square), conversation loss (red hollow square) and NF (blue solid dot) of the RF photonic receiver from the L-band to the Ka-band.

3.2 Monolithic integrated microwave photonic transceiver

The schematic diagram of the integrated RF photonic frontend based on the silicon waveguide technology, shown in Figure 17, consists of the basic function of up-conversion to the optical domain, the signal processing and the down-conversion to the electrical domain. The

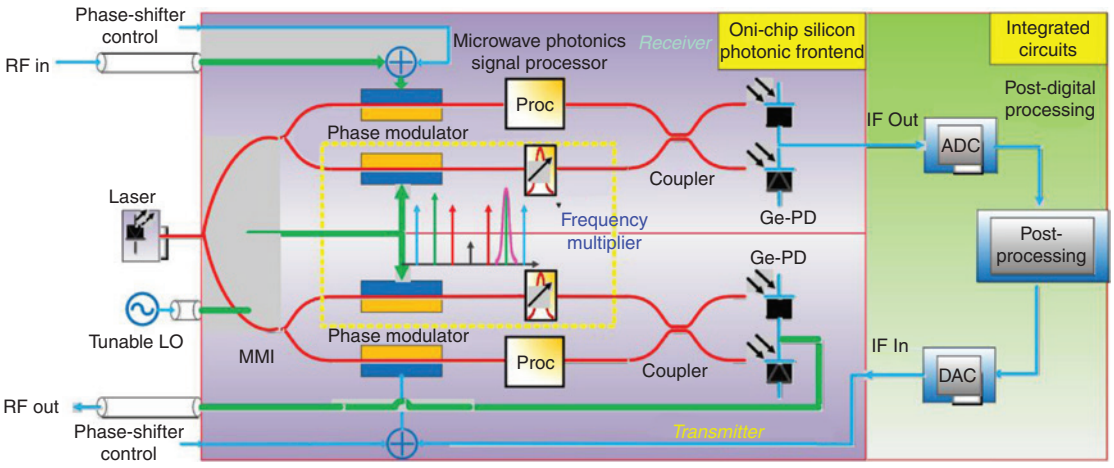

Figure 17: The schematic diagram of the fully integrated RF photonic transceiver without the on-chip laser, which consists of the transmitter and the receiver on a single silicon chip.

transmitter and the receiver are designed on the same chip with a shared CW laser as the optical carrier. For the transmitter, the signal to be transmitted from the digital system and LO were up-converted to the optical domain based on the on-chip PM modulators. After the optical LO sideband was selected by the micro-ring resonator, the modulated signal and the selected LO were mixed at the BPD. Thus, the signal with message can be down-converted to the RF domain and then transmitted to the free space through the antenna. For the receiver, it has the same scheme with the proposed full-band RF photonic receiver introduced in Section 3.1, except that the single micro-ring filter is replaced by the EIT-like signal processor to achieve a narrower bandwidth.

The chip was fabricated using the IMEC active platform through the multi-project wafer (MPW) service [28]. The modulators on the chip included a travelling wave phase modulator with a 3 dB EO bandwidth of 10 GHz at the bias voltage of –2 V, and a total length of 1.5 mm. The BPD consists of two Ge-doped PDs with a 3 dB bandwidth of 15 GHz at –1 V bias across the C-band for TE mode. The signal processor consists of an EIT-like filter and a single micro-ring filter as a channelizer filter with an FSR of about 8 nm. The uniformed curved grating couplers were used for the input and output coupling to the fibers. The insertion loss of the fiber-to-fiber via the grating coupler was measured to be 5 dB. The photomicrograph of all the fabricated devices on the chip and the picture of the measurement set-up are shown in Figure 18.

In the experiment, the performance of the transmitter on the different orders of the modulated LO sideband was measured. By tuning the frequency of the LO, the frequency of the transmitted signal can be changed from 2 GHz to 10 GHz based on the first-, second- and third-order LO sideband. As shown in Figure 19, the corresponding up-conversion gain of the first order of the LO is the highest one, whereas the second order is 5 dB lower at the low-frequency range and almost the same at 10 GHz

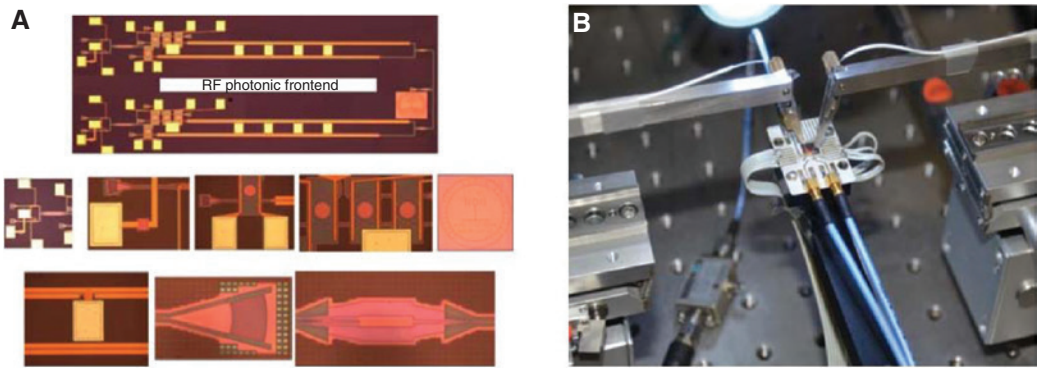

Figure 18: The experimental demonstration of the on-chip RF photonic transceiver. (A) The micrograph of the fabricated transceiver and the single devices of the BPD, IIR filter, grating coupler and 3 dB coupler; (B) The packaged device and the measurement set-up.

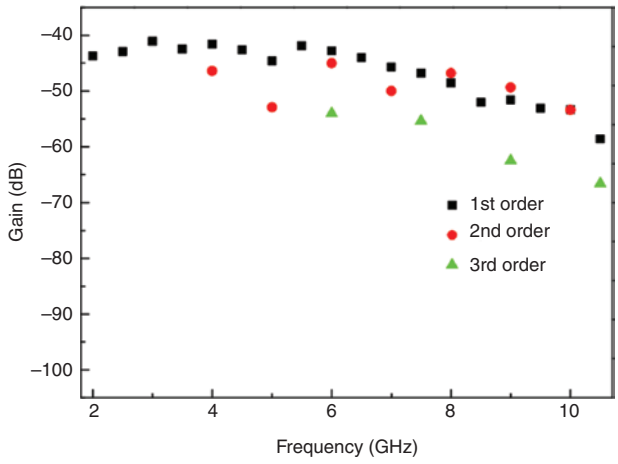

Figure 19: The measured conversion gain of the integrated RF photonic transmitter with different order of the LO.

as the first order. Although the up-conversion gain of the third order was 10 dB lower in average, it could reduce the required LO frequency to one-third of the required frequency based on the first order of the LO. For the receiver, we experimentally demonstrate that the system can accurately receive the signal from 2 GHz to 15 GHz. The corresponding SFDRs with different orders of the LO sideband were also measured across the frequency range, as shown in Figure 20, with a noise floor of around –152 dBm/Hz. The difference of about 10 dB-Hz$^{2/3}$ between the first- and third-order LO mainly comes from the down conversion gain. The degradation with the rising frequency is caused by the bandwidth of the modulation. It is notable that the SFDR of the on-chip system is more than 20 dB-Hz$^{2/3}$ lower than the proposed full-band receiver introduced in Section 3.1. The main reason is the relatively high insertion loss of the silicon platform and high nonlinearity of the on-chip modulator.

We further performed the experiment to receive two kinds of OFDM signal with signal bandwidths of 40 MHz and 400 MHz, respectively. The two kinds of OFDM signals have 97 subcarriers modulated in the form of quadrature amplitude modulation (QAM), which respectively represent the 4G signal and one of the possible 5G signal in the future. The on-chip system receives the OFDM signal with the highest rate of 1.6 Gbps, which can be widely used in the future wireless communication.

In summary, our recent works on microwave photonics are presented both on discrete devices and monolithic optical system. For the former, it can be used as receiver in radar, wireless communications and so on, with the tunability, full-band signal processing range and the immunity to EMI. For the latter, it is a good proof-of-concept silicon-based fully integrated microwave photonics front, and many efforts should be exerted to improve the performance of on-chip single devices. For example, the linearity of the silicon-based PM modulator should be improved, the propagation loss should be further lowered and the micro-ring resonators should be optimized.

4 All-optical OFDM de-multiplexer

The optical orthogonal frequency division multiplexing (OFDM) technique has been widely used in communication, such as passive optical network (PON) [49–52]. However, the electronic processing devices applied in the OFDM system are suffering from the bottleneck because of the speed limit and the high-power consumption of the analog-digital converter (ADC), the digital-analog converter (DAC) and the digital signal processor (DSP). With the advantages of high speed, large bandwidth and low power consumption, the all-optical OFDM system

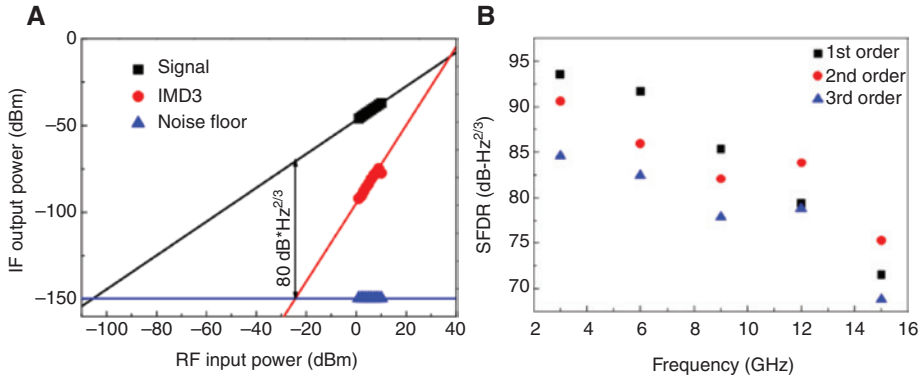

Figure 20: The experimental result of the on-chip RF photonic transceiver. (A) The measured SFDR of the on-chip system with a signal frequency of 3.435 GHz and second-order LO of 3 GHz; (B) The measured SFDR at different orders of the LO with the frequency range from 2 GHz to 15 GHz.

has the potential to break the bottleneck. In the scheme of all-optical OFDM systems, the optical inverse discrete Fourier transformer (OIDFT) and optical discrete Fourier transformer are the key elements. The all-optical OFDM systems based on different optical devices, such as the fiber Bragg grating, the highly nonlinear fiber generated optical frequency comb and the arrayed grating waveguide (AWG) on planner waveguide platform, have been proposed and experimentally demonstrated [53–56]. Among various schemes, the integrated all-optical OFDM system has great research value with the development of integrated photonics technology due to the compactness, stability and very low cost in large volume. Kang et al. [57] and Takiguchi et al. [58] proposed the all-optical DFT devices based on the N*N multimode interference. A DFT circuit based on a serial-parallel filter implemented on the cascaded MZIs with M-port MMI couplers has also been studied [59]. Here, we review our recent work on an all-OFDM de-multiplexer based on SOI technology platform.

The schematic diagram of the proposed eight-channel OFDM de-multiplexer is shown in the dashed box of Figure 21, which consists of seven asymmetric MZIs. For the single channel, it has the same architecture as the three-stage cascaded MZI-based FIR processor presented in Section 2.1. Thus, the eight-channel OFDM de-multiplexer can be considered as a system that is made up of 8 three-stage FIR processors in parallel with the fixed phase relationship. It has been demonstrated that the produced subcarriers from the OFDM de-multiplexer at each channel are orthometric in the time domain and that the eight-channel OFDM de-multiplexer is equivalent to an eight-point DFT [60].

The proposed on-chip OFDM de-multiplexer was fabricated on the SOI waveguide technology offered by LETI, as shown in Figure 22, and is based on the same process design kit (PDK) as the FIR processor in Section 2.1. The fabricated OFDM de-multiplexer has eight channels with a spacing of 8 GHz, with the total size of about 3.5 mm × 1 mm, as shown in Figure 22. The differential path lengths of the MZIs at each stage are about 8.6 mm, 4.3 mm and 2.15 mm, respectively, corresponding to the time delays of 62.5 ps, 31.25 ps and 15.625 ps. The heaters are added on the top of the short arm of each stage to achieve the phase condition by thermally tuning.

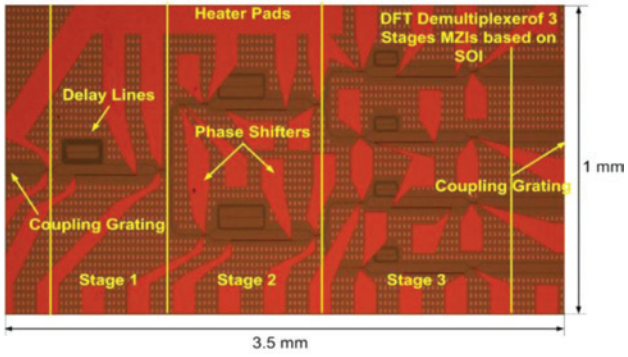

Figure 22: The fabricated OFDM de-multiplexer with eight channels based on the SOI technology.

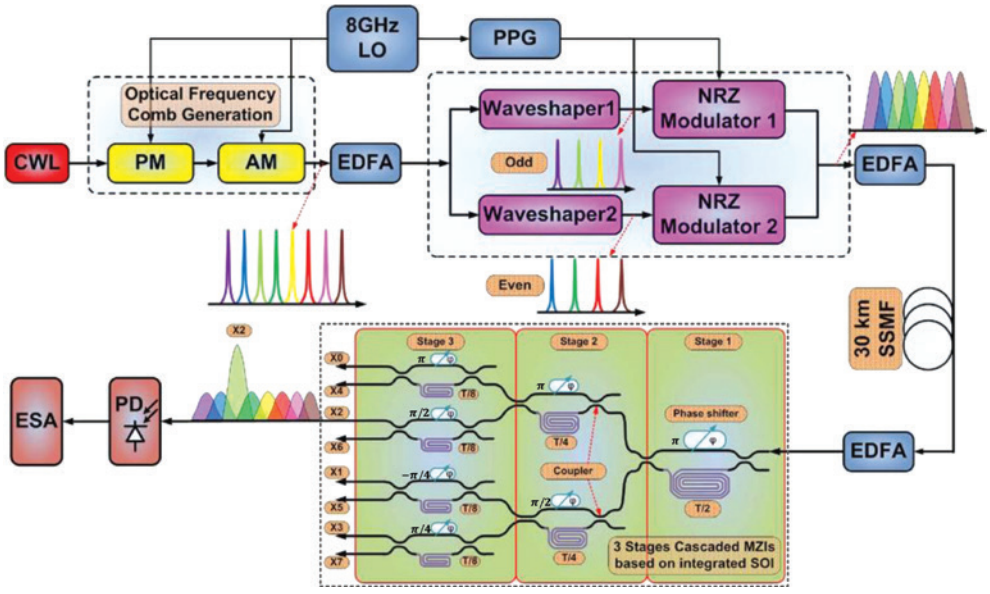

Figure 21: The schematic diagram of the all-optical OFDM communication system with the demonstrated on-chip OFDM de-multiplexer, which is shown in the dashed box.

In the experiment, the transmission spectra of the eight channels were measured by OVA. The results mostly agree well with the simulation results, as shown in Figure 23. The distortion of the transmission spectrum and the decreased extinction ratio of about 5 dB compared to the simulation may come from the large insertion loss and the fabrication error caused local phase mismatching. The grating couplers were used for the coupling to the fiber with a fiber-to-fiber loss of about 10 dB.

To further investigate the performance of the proposed OFDM de-multiplexer, an all-optical OFDM communication experiment was performed. Th block diagram of the system is shown in Figure 21. Based on a CW laser, a strong LO, a PM and AM modulators, the optical frequency comb at the central wavelength of 1550 nm are generated as the OFDM carrier with a sub-carrier spacing of 8 GHz. The frequency comb was divided into odd and even parts to be modulated by different PRBS data with 8 G-baud/s in NRZ format, so that the total rate of the system was 64 Gbps. The two parts were combined again to obtain the all-optical OFDM signal. After propagating through a 30-km single-mode fiber, the signal was sent to the on-chip de-multiplexer. All the EDFAs in the experiment link were needed to keep the signal at appropriate power level. The measured spectrum of the extracted signal at each channel suggested that the on-chip OFDM de-multiplexer could de-multiplex the subcarrier precisely with the signal-to-noise ratio (SNR) of more than 10 dB, as shown in Figure 24A. The bit error rate (BER) of the system was also measured by a pulse pattern generator on the condition of back-to-back and after-30-km single mode fiber transmission, as shown in Figure 24B. All the results are below the forward error correction (FEC) limit when the received power is from 3 dBm to –3 dBm. The power penalty is about 2 dB when the received power is –3 dBm after the transmission, which is mainly from the chromatic dispersion of the optical fiber and the insertion loss of the on-chip system. This work demonstrates the effectiveness of the on-chip all-optical OFDM de-multiplexer, which has the potential to be used in the all-optical OFDM system, especially in the mobile system due to the compactness.

Compared with the reported integrated DFT-based all optical OFDM de-multiplexers shown in Table 1, our work has the advantage of footprint due to the high

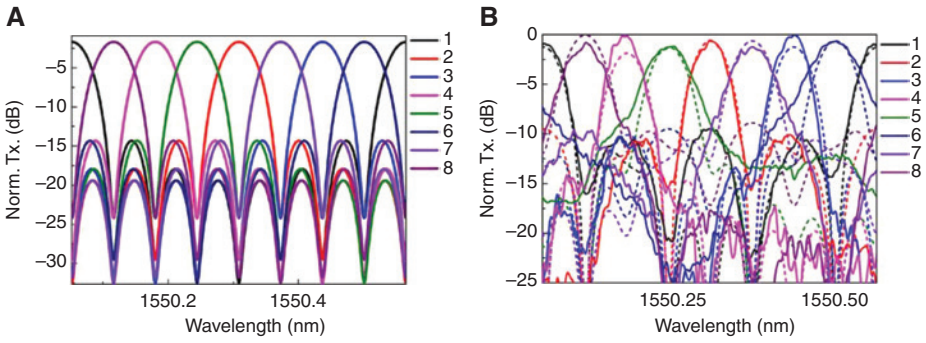

Figure 23: The transmission spectra of the on-chip OFDM de-multiplexer with the channel spacing of about 8 GHz. (A) The simulated result and (B) the measured result.

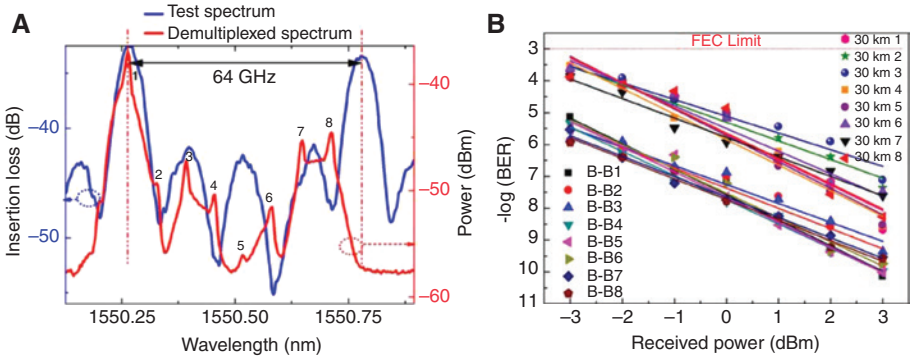

Figure 24: The experimental result of the all-optical OFDM communication. (A) The received signal spectrum at the X2 subcarrier from the output of the on-chip OFDM de-multiplexer. (B) The BERs of the eight subcarriers for back-to-back (B-B) and after 30 km transmissions in the all-optical OFDM communication experiment.

Table 1: Comparison of different reported integrated DFT-based all optical OFDM de-multiplexers.

Reference	FSR (GHz)	Number of channels	Demonstrated transmission capacity	Chip Size	Technology
This work	64	8	8×8 Gbps	3.5 mm×1 mm	SOI
[57]	40	8	13×20 Gbps	30 mm×8 mm	PLC
[58]	40	4	4×10 Gbps	21 mm×25 mm	PLC
[59]	100	8	8×13.5 Gbps	8 mm×13.5 mm	SOI

compactness of SOI technology and similar performance on the channels. However, the demonstrated transmission capacity of all optical OFDM communication is lower than in some works because we just used a simple modulation format in the experiment. In a further study, we will try to improve the transmission capacity on the chip by introducing a complex modulation format and other multiplexing methods.

5 High resolution spatial heterodyne spectrometer

With the rapid development of the Internet of things, the biomedical sensing and the space missions promoted by private space industry, monolithic spectrometers are vastly needed in these fields due to the irreplaceable advantages of miniaturization [61]. Here, our recent work on the integrated spatial heterodyne spectrometer (SHS) based on the TriPleX™ technology is reviewed [62]. It has the advantage of large optical throughput and a good balance among high resolution, fabrication tolerance and cost compared with other different schemes of on-chip spectrometer [63, 64].

The on-chip SHS with k channels is comprised of k MZIs in parallel, of which the kth MZI has a differential path length of $(k-1)\cdot\Delta L$, as shown in Figure 25. We have demonstrated that the transmission function of the on-chip system has the same mathematical form as the discrete cosine transform (DCT) under a certain condition [62]. This means that the output of the on-chip SHS is the DCT of the discretized spectrum of the input signal. By using the linear CCD to detect the output power at each MZI and measuring the transmission matrix in advance, we can obtain the discretized spectrum through the inverse computation. The mathematical derivation also suggests that the resolution of the SHS system is one half of the FSR of the MZI with the longest differential path length, whereas the signal processing range is one half of the FSR of the MZI with the shortest differential path length. The device was fabricated with 8 MZIs based on

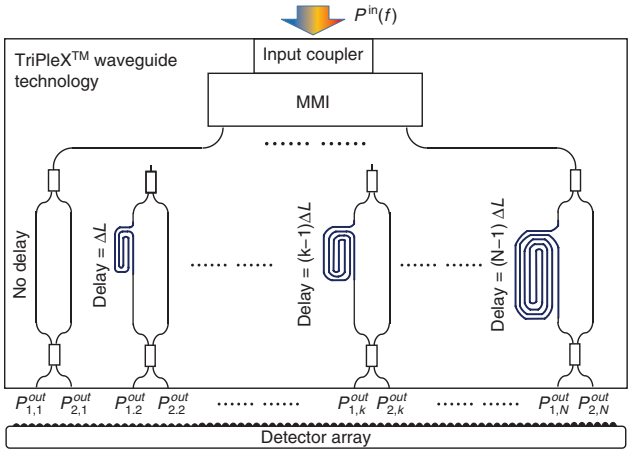

Figure 25: The schematic diagram of the on chip SHS with N channels based on the arrayed MZIs.

the double-strip TriPleX™ waveguide platform, with a size of 8 mm×4mm, as shown in Figure 26A. The respective differential path lengths of the 8 MZIs were designed to be 0, 4.3 mm, 2×4.3 mm, ... and 7×4.3 mm. Hence, the resolution of the on-chip system was estimated to be around 20 pm with the group index of 1.71 at the central wavelength of 1550 nm.

In the experiment, the FSRs of the 2nd MZI and the 8th MZI are 0.045 nm and 0.318 nm, respectively, as shown in Figure 26B, which agree with the design. On the basis of the measured transmission spectrum of the 8 MZIs, we build the transfer matrix T of the on-chip SHS. Next, a CW tunable laser with linewidth of 100 kHz at different wavelengths was launched into the SHS. The retrieved spectra based on the SHS and the measurement results of a commercial optical spectrum analyzer are shown in Figure 27A and B. A signal consisting of two CW lights separated by 23 pm was also launched into the SHS and could be retrieved accurately, as shown in Figure 27C. This suggests that the on-chip system has a resolution of 23 pm at the wavelength of about 1550 nm. Figure 27D shows the retrieved spectrum of a signal with a spectrum in the Gaussian profile, with a full width at half maximum of 90 pm. This result is in accordance with the measurement

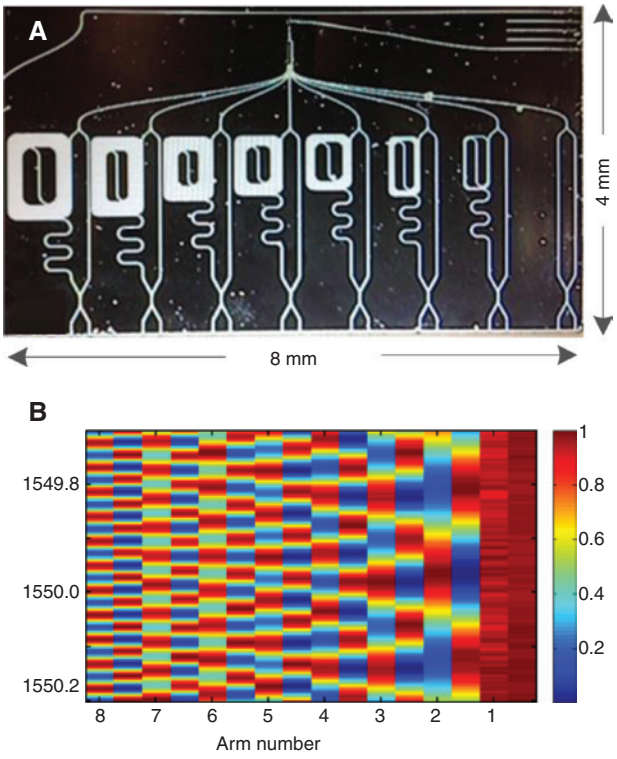

Figure 26: The experimental demonstration of the on chip SHS. (A) The fabricated SHS with eight channels based on the TriPleX™ waveguide technology. (B) The measured transmission spectra at the two output ports of the 8 MZIs.

result of the commercial device. All the experiment results demonstrate the good performance of the on-chip SHS on the spectroscopic analysis.

Until now, the reported work on the on-chip SHS are mainly fabricated on the SOI technology platform and the planar lightwave circuit (PLC) technology platform [61, 64–66]. For the former, the relatively large loss of the SOI technology limits the resolution of the SHS so that there is no reported device with a resolution of less than 40 pm. It has been demonstrated that if the propagation loss is about –2 dB/cm to –4 dB/cm, the maximum path difference of the MZI must be less than 2.5 cm to 1.25 to achieve a good performance on SNR. Such a length range corresponds to a resolution of 20 pm to 40 pm at the wavelength of 1550 nm on the SOI platform [62]. For the latter, the reported device can realize a high resolution of 8 pm, but the chip size would be very large due to the bend radius of the waveguide is of order of millimeters. Some of the reported works on the on-chip SHS are shown in Table 2.

To the best of our knowledge, this work is the first time to experimentally demonstrate the on-chip SHS on Si_3N_4/SiO_2 waveguide platform. This platform combines the advantages of the SOI technology and PLC technology. Thus, it has the potential to achieve a very high resolution of 1 pm in a compact size based on the Si_3N_4/SiO_2 waveguide platform. The proposed on-chip SHS can be widely

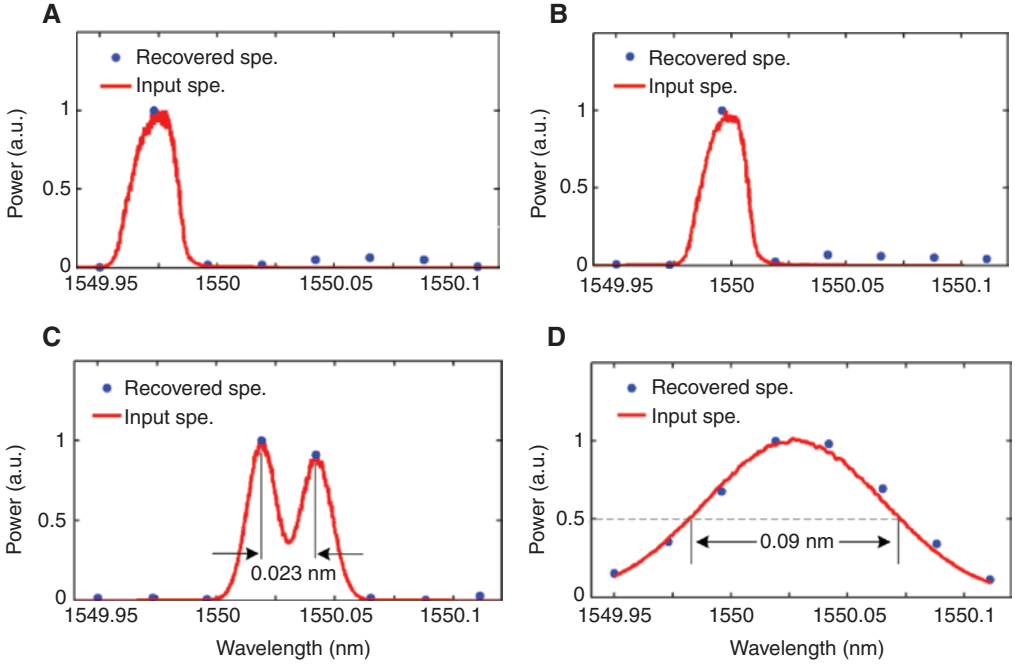

Figure 27: The recovered spectra (blue dot) by the on-chip SHS in different input signals. (A) and (B) a CW signal at wavelengths of 1549.970 nm and 1550.001 nm, respectively; (C) two CW signals separated by 0.023 nm at wavelengths of about 1550.025 nm, respectively; (D) signal in the Gaussian line shape with a FWHM of 0.09 nm. For comparison, the input signals were measured by a commercial optical spectrum analyzer shown by the red line.

Table 2: Comparison of different reported on-chip spatial heterodyne spectrometers.

Reference	Resolution (pm)	Bandwidth @ center wavelength (nm)	Chip size	Loss of waveguide (dB/cm)	Technology
This work	23	184 pm @ 1550	4 mm × 8 mm	~0.1	TriPleX™
[61]	50	2.5 nm @ 1365	40 mm × 60 mm[a]	~2	SOI
[65]	40	750 pm @ 1550	12 mm^2	~4	SOI
[64]	50	780 pm @ 1550	4 mm × 6 mm	~3.1	SOI
[66]	8	512 pm @ 1550	–	~0.02	PLC

[a]We estimated the data were from the photo in the reference [61].

used in the fields of space exploration, biosensing and so on, from visible to infrared light.

6 Conclusion

We have presented our works on the optical signal processing on-chip system based on the silicon or silicon nitride photonics waveguide platform. Three types of optical signal processor are investigated and compared, which are built on the two basic elements of MZI and the micro-ring resonator. For the FIR processor, it has the advantages of linear phase response and reconfigurability, although it has a relatively smaller FSR. For the IIR processor, it can achieve high resolution with compact size and large FSR, but it is sensitive to the fabrication tolerance. For the EIT-like signal processor, it has the potential to achieve a very high Q factor.

With these building blocks, we further present different optical signal processing systems in the applications of microwave photonics, all-optical OFDM communications and spectrograph. For the RF front receiver, a signal processing range of full-band was realized. Further works will focus on improving the rectangle coefficient of the on-chip signal processor and reducing the total insertion loss of the system. For the fully integrated RF transceiver, the received signal range is up to about 10 GHz, but the SFDR is relatively low. The two systems can be used in the next generation of radar and also in the 5G wireless communications. Most of the limitations come from the loss of the silicon waveguide and the relatively high nonlinearity of the modulator caused by the abundant nonlinear effects of silicon. More efforts should be devoted to solving these problems. For the on-chip OFDM de-multiplexer, this has been demonstrated with an all-optical OFDM communication system with the rate of 64 Gbps. This work is especially suitable for exploring the optical access network due to its compact size and very low cost in large volumes. In our further study, the main effort will focus on reducing the insertion loss of the SOI-based circuit and realizing the de-multiplexer on the low-loss Si_3N_4 waveguide platform to improve the BER. Furthermore, a de-multiplexer with more channels is another research topic to explore in improving the band rate. We also show a monolithic SHS with a high resolution of about 20 pm based on the low loss Si_3N_4/SiO_2 waveguide technology, which can be widely used in the fields of health care, smart devices and space exploration. Further improvements on the SHS will focus on increasing the number of channels and the path length to realize a wider bandwidth and higher resolution. In addition, thermal tuning on the transmission function of the MZI is another way to increase the bandwidth without increasing the amount of the MZIs.

The most important remaining problem for the microsystems presented in this paper is the lack of an integrated laser. One promising method relies on the hybrid integration technology. In this method, the III/V material is used for the optical gain on the silicon platform or silicon nitride platform by butt coupling or wafer bonding to build an on-chip laser. For example, a record-narrow integrated laser with a linewidth of 290 Hz based on the Si_3N_4/InP hybrid waveguide platform has been experimentally demonstrated recently [67].

Acknowledgments: The authors would thank LioniX BV for offering the TriPleX™ waveguide technology, and the IMEC and LETI for offering the SOI waveguide technology. Our works are partially supported by the National Natural Science Foundation of China (NSFC) under Contract no. 61771285 and 61335002, Funder Id: 10.13039/501100001809.

References

[1] M. M. Waldrop, Nature 530.7589, 144–147 (2016).
[2] M. Smit, J. J. G. M. Van der Tol and M. Hill, Laser Photon. Rev. 6, 1–13 (2012).
[3] J. E. Bowers and A. Y. Liu, In 'Optical Fiber Communication Conference', Los Angeles, CA, USA, (2017) M2B. 4.
[4] M. N. Sysak, in 'Optical Fiber Communication Conference', Los Angeles, CA, USA, (2015) Th1G. 3.

[5] S. Assefa, S. Shank, W. Green, M. Khater, E. Kiewra, et al., in 'IEEE International Electron Devices Meeting (IEDM)', San Francisco, CA, USA, (2012) pp. 33.8.1–33.8.3.
[6] D. J. Goodwill, in 'Optical Fiber Communications Conference and Exhibition (OFC)', Los Angeles, CA, USA, (2017) pp. 1–3.
[7] M. Hochberg and T. Baehr-Jones, Nature Photon. 4, 492–494 (2010).
[8] A. E.-J. Lim, J. Song, Q. Fang, C. Li, X. Tu, et al., IEEE J. Sel. Topics Quantum Electron. 20, 405–416 (2014).
[9] P. Dumon, W. Bogaerts, R. Baets, J.-M. Fedeli and L. Fulbert, Electronics Lett. 45, 581–582 (2009).
[10] M. K. Smit, X. J. M. Leijtens, E. A. J. M. Bente, J. J. G. M. van der Tol, H. P. M. M. Ambrosius, et al., in 'Optical Fiber Communication Conference', Los Angeles, CA, USA, (2012) OM3E.3.
[11] A. Leinse, H. Leeuwis, A. Prak, R. G. Heideman, A. Borst, et al., in '2011 ICO International Conference on Information Photonics (IP)', Ottawa, ON, Canada, (2011) pp. 1–2.
[12] J. Liow, M. Yu, P. Lo, D. Kwong, in 'IEEE International Conference Solid-State and Integrated Circuit Technology (ICSICT)', Shanghai, China, (2010), pp. 29–32.
[13] R. Soref, D. Buca and S.-Q. Yu, Optics and Photonics News 27, 35 (2016).
[14] A. Ribeiro, A. Ruocco, L. Vanacker and W. Bogaerts, Optica 3, 1348–1357 (2016).
[15] J. Sun, E. Timurdogan, A. Yaacobi, E. S. Hosseini and M. R. Watts, Nature 493, 195 (2013).
[16] C. Sun, M. T. Wade, Y. Lee, J. S. Orcutt, L. Alloatti, et al., Nature 528, 534–538 (2015).
[17] C. Zhang, S. Zhang, J. D. Peters and J. E. Bowers, Optica 3, 785–786 (2016).
[18] Y. Shen, N. C. Harris, M. Prabhu, T. Baehr-Jones, M. Hochberg, et al., Nature Photon. 11, 441–446 (2017).
[19] D. Marpaung, B. Morrison, M. Pagani, R. Pant, D.-Y. Choi, et al., Optica 2, 76–83 (2015).
[20] L. Zhuang, C. G. H. Roeloffzen, M. Hoekman, K.-J. Boller and A. J. Lowery, Optica 2, 854–859 (2015).
[21] W. Liu, M. Li, R. S. Guzzon, E. J. Norberg, J. S. Parker, et al., Nature Photon. 10, 190–195 (2016).
[22] C. K. Madsen and J. H. Zhao, in 'Optical Filter Design and Analysis: A Signal Processing Approach John Wiley & Sons', Ed. By K. Chang (Inc. US, New York, 1999).
[23] P. Toliver, R. C. Menendez, T. C. Banwell, A. Agarwal, T. K. Woodward, et al., in 'Optical Fiber Communication Conference', San Diego, CA, USA, (2010) OWJ4.
[24] N. Takato, T. Kominato, A. Sugita, K. Jinguji, H. Toba, et al., IEEE J. Sel. Areas Commun. 8, 1120–1127 (1990).
[25] S. S. Djordjevic, L. W. Luo, S. Ibrahim, N. K. Fontaine, C. B. Poitras, et al., IEEE Photon. Technol. Lett. 23, 42–44 (2011).
[26] H. Yu, M. Chen, P. Li, S. Yang, H. Chen, et al., Opt. Exp. 21, 6749–6755 (2013).
[27] H. Yu, P. Li, M. Chen, S. Yang, H. Chen, et al., in 'Opto Electronics and Communications Conference held jointly with 2013 International Conference on Photonics in Switching (OECC/PS)', Kyoto, Japan, (2013), pp. 1–2.
[28] P. P. Absil, P. De Heyn, H. Chen, P. Verheyen, G. Lepage, et al., Proc. SPIE. 9367, 93670V (2015).
[29] K. Wörhoff, R. G. Heideman, A. Leinse and M. Hoekman, Adv. Opt. Technol. 4, 189–207 (2015).
[30] H. Yu, M. Chen, Q. Guo, M. Hoekman and H. Chen, et al., IEEE Photon. J. 7, 1–9 (2015).
[31] W. Bogaerts, P. De Heyn, T. Van Vaerenbergh, K. De Vos, S. Kumar Selvaraj, et al., Laser Photon. Rev. 6, 47–73 (2012).
[32] C.-H. Dong, L. He, Y.-F. Xiao, V. R. Gaddam, S. K. Ozdemir, et al., Appl. Phys. Lett. 94, 231119 (2009).
[33] L.-D. Haret, T. Tanabe, E. Kuramochi and M. Notomi, Opt. Exp. 17, 21108–21117 (2009).
[34] Q. Xu, D. Fattal and R. G. Beausoleil. Opt. Exp. 16, 4309–4315 (2008).
[35] M. Notomi, T. Tanabe, A. Shinya, E. Kuramochi, H. Taniyama, et al., Opt. Exp. 15, 17458–17481 (2007).
[36] D. K. Armani, T. J. Kippenberg, S. M. Spillane and K. J. Vahala, Nature 421, 925 (2003).
[37] H. Yu, H. Yu, J. Wang, M. Chen, M. Hoekman, et al., in 'Optical Fiber Communications Conference and Exhibition (OFC)' Anaheim, CA, USA, (2016), Th2A.19.
[38] H. Yu, M. Chen, Q. Guo, M. Hoekman, H. Chen, et al., J. Lightw. Technol. 34, 701–706, (2016).
[39] Q. Xu, S. Sandhu, M. L. Povinelli, J. Shakya, S. Fan, et al., Phys. Rev. Lett. 96, 123901 (2006).
[40] M. H. Khan, H. Shen, Y. Xuan, L. Zhao, S. Xiao, et al., Nature Photon. 4, 117–122 (2010).
[41] M. Carter, B. Lazareff, D. Maier, J.-Y. Chenu, A.-L. Fontana, et al., Astron Astrophys. 538, A89 (2012).
[42] J. Capmany and D. Novak, Nature Photon. 1, 319–330 (2007).
[43] Y. Jianping and J. Lightw, Technol. 27, 314–335 (2009).
[44] P. Ghelfi, F. Laghezza, F. Scotti, G. Serafino, A. Capria, et al., Nature 507, 341 (2014).
[45] J. D. McKinney, Nature 507, 310–312 (2014).
[46] D. Marpaung, C. Roeloffzen, R. Heideman, A. Leinse, S. Sales, et al., Laser Photon. Rev. 7, 506–538 (2013).
[47] A. Kanno, K. Inagaki, I. Morohashi, T. Sakamoto, T. Kuri, et al., Opt. Exp. 19, B56–B63 (2011).
[48] C. G. Roeloffzen, L. Zhuang, C. Taddei, A. Leinse, R. G. Heideman, et al., Opt. Exp. 21, 22937–22961 (2013).
[49] W. Shieh, H. Bao and Y. Tang. Opt. Exp. 16, 841–859 (2008).
[50] Z. Yu, X. Yi, J. Zhang, D. Zhao, K. Qiu, et al., J. Lightw. Technol. 32, 3926–3931 (2014).
[51] Z. Yu, X. Yi, Q. Yang, M. Luo, J. Zhang, et al., Opt. Exp. 21, 3885–3890 (2013).
[52] E. Giacoumidis, X. Q. Jin, A. Tsokanos and J. M. Tang, IEEE Photon. J. 2, 130–140 (2010).
[53] H. Chen, M. Chen and S. Xie, J. Lightw. Technol. 27, 4848–4854 (2009).
[54] D. Hillerkuss, R. Schmogrow and J. Leuthold, Nature Photon. 5, 364–371 (2011).
[55] C. R. Doerr and K. Okamoto, J. Lightw. Technol 24, 4763–4789 (2006).
[56] A. J. Lowery, Opt. Exp. 18, 14129–14143 (2010).
[57] I. Kang, X. Liu, S. Chandrasekhar, M. Rasras, H. Jung, et al., Opt. Exp. 20, 896–904 (2012).
[58] K. Takiguchi, T. Kitoh, M. Oguma, Y. Hashizume, H. Takahashi, et al., in 'Optical Fiber Communication Conference', Los Angeles, CA, USA, (2012) OM3J–6.
[59] A. Rahim, S. Schwarz, J. Bruns, K. Voigt, G. Winzer, et al., IEEE Photon. Technol. Lett. 25, 1977–1980 (2013).
[60] D. Hillerkuss, M. Winter, M. Teschke, A. Marculescu, J. Li, et al., Opt. Exp. 18, 9324–9340 (2010).
[61] M. Florjańczyk, C. Alonso-Ramos, P. Bock, A. Bogdanov, P. Cheben, et al., Optical and Quantum Electronics 44, 549–556 (2012).

[62] Y. Li, H. Yu, L. An, Q. Guo, M. Chen, et al., IEEE Photon. Technol. Lett. 28, 2712–2715 (2016).
[63] J. M. Harlander, J. E. Lawler, J. Corliss, F. L. Roesler and W. M. Harris, Opt. Exp. 18, 6205–6210 (2010).
[64] P. J. Bock, P. Cheben, A. V. Velasco, J. H. Schmid, A. Delage, et al., Laser Photonics Rev. 7, L67–L70 (2013).
[65] A. V. Velasco, P. Cheben, M. Florjańczyk, J. H. Schmid, P. J. Bock, et al., Opt. Lett. 38, 706–708 (2013).
[66] N. K. Fontaine, K. Okamoto, T. Su and S. J. B. Yoo, Opt. Lett. 36, 3124–3126 (2011).
[67] Y. Fan, R. M. Oldenbeuving, C. G. Roeloffzen, M. Hoekman, D. Geskus, et al., in 'CLEO: Applications and Technology', San Jose, CA, USA, (2017) JTh5C. 9.